Available online at www.sciencedirect.com

ScienceDirect

Acta Materialia 70 (2014) 281–289

Acta MATERIALIA

www.elsevier.com/locate/actamat

The five-parameter grain boundary character and energy distributions of a fully austenitic high-manganese steel using three dimensional data

Hossein Beladi [a,*], Noel T. Nuhfer [b], Gregory S. Rohrer [b]

[a] Institute for Frontier Materials, Deakin University, Geelong, VIC 3216, Australia
[b] Department of Materials Science and Engineering, Carnegie Mellon University, Pittsburgh, PA 15213-3890, USA

Received 9 November 2013; received in revised form 26 February 2014; accepted 26 February 2014

Abstract

The three-dimensional interfacial grain boundary network in a fully austenitic high-manganese steel was studied as a function of all five macroscopic crystallographic parameters (i.e. lattice misorientation and grain boundary plane normal) using electron backscattering diffraction mapping in conjunction with focused ion beam serial sectioning. The relative grain boundary area and energy distributions were strongly influenced by both the grain boundary plane orientation and the lattice misorientation. Grain boundaries terminated by (1 1 1) plane orientations revealed relatively higher populations and lower energies compared with other boundaries. The most frequently observed grain boundaries were {1 1 1} symmetric twist boundaries with the Σ3 misorientation, which also had the lowest energy. On average, the relative areas of different grain boundary types were inversely correlated to their energies. A comparison between the current result and previously reported observations (e.g. high-purity Ni) revealed that polycrystals with the same atomic structure (e.g. face-centered cubic) have very similar grain boundary character and energy distributions.

Keywords: Grain boundary energy; Microstructure; TWIP steel; Electron backscattering diffraction; Focused ion beam

1. Introduction

A new generation of high-manganese steels has recently received significant attention among research groups worldwide as these steels offer an outstanding mechanical property balance (e.g. a high strength of ~1 GPa and high ductility of ~60% [1]). The unique combination of properties was attributed to the formation of nanosized (i.e. 20–50 nm) mechanical twins during deformation, which retards the onset of necking and consequently enhances both strength and ductility. This phenomenon is referred to as twinning-induced plasticity (TWIP). Mechanical twin formation is common in austenitic materials with low stacking fault energy (SFE) in the range 20–50 mJ m^{-2} [2].

Similar to other phase transition phenomena, the formation of mechanical twinning consists of nucleation and growth processes, which are both controlled by the dislocation substructure characteristics [3,4]. Kamaran et al. [5] argued that the activation of multiple slip systems and the existence of dislocation pile-ups are prerequisites for mechanical twin formation. Interestingly, mechanical twinning mostly nucleates at grain boundaries and subsequently propagates across the grain [1]. This is not surprising as multiple slip mostly takes place near grain boundaries to maintain the strain compatibility between adjacent grains [6,7]. It should be noted that grain boundary properties are anisotropic, depending upon the lattice

* Corresponding author.
E-mail address: hossein.beladi@deakin.edu.au (H. Beladi).

http://dx.doi.org/10.1016/j.actamat.2014.02.038
1359-6454/

misorientation and grain boundary plane orientation [8–12]. This suggests that the grain boundary character and energy distributions may contribute somewhat to the extent of mechanical twin formation in low-SFE austenitic materials.

To quantitatively characterize the grain boundary plane distribution and energy, five independent macroscopic crystallographic parameters are required: three for the lattice misorientation and two for the orientation of the boundary plane [12]. The latter needs advanced equipment to accurately resolve the three-dimensional internal microstructures of materials. Despite the complexity of the existing three-dimensional techniques, recent developments in automated microscopy, such as the dual-beam focused ion beam scanning electron microscope (i.e. serial sectioning), have made these measurements possible. Using this technique, the geometries of grain boundaries meeting at triple junctions can be accurately resolved [8–11]. This makes it possible to measure both the grain boundary character distribution (GBCD) and the grain boundary energy distribution (GBED) as a function of all five macroscopic crystallographic parameters [8–11]. This approach was recently employed to systematically analyze the relative area and energy of grain boundaries in a limited number of polycrystalline materials with different crystal structures such as MgO [8], yttria [9], Ni [10] and ferritic steel [11]. These measurements revealed that there is a strong inverse relationship between the relative population and energy of grain boundaries for all of these polycrystalline materials [8–11]. However, the crystal structure significantly influenced the extent and characteristics of the anisotropy observed in the GBCD and GBED [8–11].

In spite of the industrial significance of austenitic TWIP steels, there is hardly any information available regarding the relative population and energy of grain boundaries for this class of materials. Although the extent of research performed on the grain boundary energy in face-centered cubic (fcc) metals is comparatively greater than other crystal structures, these measurements were performed either over a limited range of the crystallographic parameters [13–27] or on high-SFE metals (e.g. Ni [10], ~128 mJ m^{-2} [28]). The objective of the current paper is to present a comprehensive description of the grain boundary character and energy distributions in a fully austenitic high-manganese TWIP steel through the five-parameter grain boundary analysis approach using three-dimensional data obtained from serial sectioning combined with EBSD data.

2. Experimental procedure

2.1. Material

The steel composition in the current study was 0.6C–18Mn–1.5Al (wt.%). The SFE of this steel was reported elsewhere [29] to be ~25 mJ m^{-2} at room temperature [2]. This ensures that mechanical twinning takes place during deformation. Therefore, the current composition falls in the TWIP steel class. The experimental material was in the form of a sheet product with a thickness of ~1.5 mm supplied by POSCO Research Laboratory, Gwangyang, South Korea. The sheet was produced through ~60% cold rolling followed by a 1 min anneal at 800 °C, resulting in a fully recrystallized microstructure with an average grain size of ~2.5 μm.

2.2. Three-dimensional EBSD measurement

A specimen 5 mm × 4 mm was first cut from the sheet. It was then mechanically ground from both sides to produce a thin strip ~150 μm thick with parallel surfaces. 3-D EBSD measurements and serial sectioning were performed on the rolling direction–normal direction (RD–ND) plane using a FEGSEM Quanta 3D FEI scanning electron microscope. The 3-D EBSD procedure and setup were discussed in detail elsewhere [11]. In brief, 200 nm of material was removed at each serial sectioning step using a 30 kV, 3 nA Ga^{+} ion beam. The ion-milling condition was carefully selected to minimize any surface damage (e.g. mechanical twinning and/or martensite phase transformation) that might occur through serial sectioning, specifically for low-SFE austenitic materials. EBSD mapping was performed using an electron beam with a voltage of 20 kV and a current of 4 nA. The in-plane point spacing (i.e. step size) of the EBSD scans was 150 nm. The current results were collected from one 3-D EBSD run consisting of 100 slices. The total volume of the 3-D EBSD run was 65 μm × 40 μm × 20 μm, covering approximately 6300 grains.

2.3. Data processing

EBSD data were initially processed using functions in the TSL software to extract boundary line traces/segments, which were then employed to construct the triple lines, where triple points on adjacent layers were made up of crystals with the same orientation. Afterwards, the triple lines were used to calculate the relative grain boundary area and energy distributions using a five-parameter approach described in detail elsewhere [9]. The grain boundary energy calculation was performed through the capillarity vector reconstruction method demonstrated by Morawiec [30]. The current data set yielded ~67,100 triple lines. The grain boundary normal vector (i.e. grain boundary plane orientation) was calculated through the cross-product of the triple line connecting adjoining layers and the corresponding grain boundary line trace. This calculation yielded ~402,600 normal vectors.

The GBCD and GBED were analyzed discretely, with 9 bins per 90°, which offers 10° resolution. For this case, 97% of the bins contained 10 or more observations. The energy reconstruction was performed on the 67,100 triple junctions. An iterative approach was employed to reconstruct the capillarity vector, as described in Ref. [30]. In the present study, 300 iterations were used and the relaxation

factor for each iteration was 0.05. The change on the last iteration was <1% of the change on the first, which was taken as the condition for convergence.

3. Results

A reconstructed 3-D EBSD map for 100 consecutive parallel layers is shown in Fig. 1. The fully austenitic microstructure revealed a pronounced brass-type $\{1\,1\,0\}_\gamma$-$\langle 1\,1\,2\rangle_\gamma$ crystallographic texture (Fig. 2a). This is a typical texture for low-SFE fcc alloys [31]. The inverse pole figure was characterized by a relatively weak texture having a maximum of ~1.9 times random intensity (Fig. 2b).

The relative area of grain boundary planes for all misorientations, $\lambda(\mathbf{n})$, where $\mathbf{n}$ is the normal to the grain boundary plane, was drawn in the crystal reference frame (Fig. 3a). The distribution was measured in multiples of a random distribution (MRD), where values >1 specify that planes were seen more often than anticipated in a random distribution. The distribution showed strong anisotropy, with a maximum at the (1 1 1) position having a value of 2.03 MRD (i.e. the population of (1 1 1) planes was ~100% more than expected in a random distribution). By contrast, the distribution had a minimum at the (1 0 0) position with 0.75 MRD (Fig. 3a). The distribution at the (1 0 1) orientation was ~1 MRD. In parallel, the relative grain boundary energy also varied with the grain boundary plane orientation. Note that the minima and maxima of the energy distribution are opposite to the relative area distribution, with the minimum energy centring at (1 1 1) with 0.96 a.u. and the maximum at (1 0 0) with 1.1 a.u. (Fig. 3b). The energy at (1 0 1) was ~1.02 a.u.

In the current study, the relative grain boundary character and energy distributions for specific misorientations were drawn for the [1 1 1], [1 1 0] and [1 0 0] misorientation axes. The distributions were plotted in the bicrystal reference frame, where the [0 0 1] direction was placed perpendicular to the paper plane and the [1 0 0] crystal axis was pointed horizontally in the plane of the paper and to the right. Here, the grain boundary plane and energy distributions were plotted for a wide range of misorientations, using certain coincident site lattice (CSL) misorientations (i.e. Σ1, Σ3, Σ5, Σ7, Σ9, Σ11, Σ19b, Σ21a, Σ25a and, Σ33a) as reference points. The distributions of relative grain boundary plane area and energy varied remarkably as a function of misorientation.

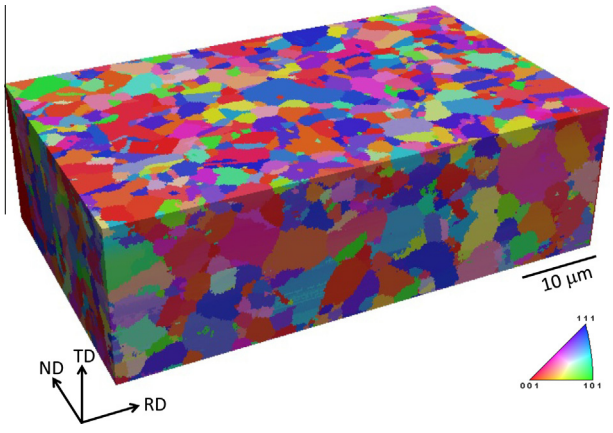

Fig. 1. Reconstructed serial sections of EBSD of the TWIP steel, containing 100 slices. RD, ND and TD are rolling direction, normal direction and transverse direction, respectively. The colours are the orientations referred to the normal direction. (For interpretation of the references to colour in this figure legend, the reader is referred to the web version of this article.)

The grain boundary plane distribution revealed a relatively strong peak at the (1 1 1) twist position for misorientations about the [1 1 1] axis ranging from 10° to 46.8° (Fig. 4a–d). The peak intensity slightly fluctuated between 2.3 and 3.8 MRD over this misorientation angle range, though it did not follow any specific trend with the misorientation angle. At a misorientation of 60°, the peak intensity at the (1 1 1) pure twist position significantly increased with a pronounced population of approximately 500 MRD (Fig. 5a). The $\{1\,1\,1\}\|\{1\,1\,1\}$ symmetric twist grain boundaries represent the coherent twin for the Σ3 misorientation in fcc materials [12], having the highest grain boundary population in the distribution.

The distribution of grain boundary energy for a [1 1 1]-type misorientation axis as a function of misorientation angle revealed a similar trend to that observed in the corresponding GBCD (Figs. 4 and 5). On average, the grain boundaries with the lower populations were observed to have the maximum energy and those with the minimum energy were more frequently populated. However, this was not always the case. For example, the (1 1 1) symmetric twist position always showed the maximum in the grain boundary population for all misorientation angles (Figs. 4a–d and 5a). Most of the energy distributions showed a minimum at these positions (Figs. 4e, f and 5b) but exceptions occurred at Σ7 and Σ19b (Fig. 4g and h) The inverse correlation was most pronounced and obvious at a misorientation angle of 60°, where the lowest energy is observed at the position of the (1 1 1) pure symmetric twist boundary which also has the highest population (i.e. Σ3, Fig. 5). It is notable that the inverse correlation is strongest at the positions where we have the most observations.

The distribution of grain boundary planes for the [1 1 0] misorientation axis changed significantly as a function of misorientation angle. The common feature for all distributions, however, was the absence of twist boundaries, as evidenced by the minimum at the {1 1 0} twist boundary position (Fig. 6a–c). Multiple peaks appeared in the grain boundary distribution for a misorientation angle of 20°, having modest maxima of ~1.75 MRD. The two main peaks were located on the zone of pure tilt boundaries (i.e. the great circle perpendicular to [1 1 0], Fig. 6a). For this misorientation, the symmetric tilt boundaries are the $(4\,{-}4\,1)\|(4\,{-}4\,1)$ and $(1\,{-}1\,8)\|(1\,{-}1\,8)$ positions, marked in Fig. 6a. Therefore, the maxima in the [1 1 0] zone represent asymmetric tilt boundaries. The distribution of grain boundary planes was significantly

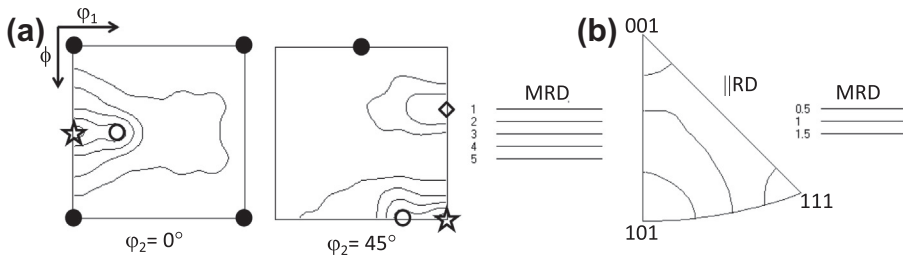

Fig. 2. (a) Orientation distribution function of the TWIP steel and (b) inverse pole figure of the steel along the rolling direction (RD). MRD is multiples of a random distribution. (○) brass {011}⟨211⟩; (●) cube {100}⟨001⟩; (☆) goss {011}⟨100⟩; (◇) copper {112}⟨111⟩.

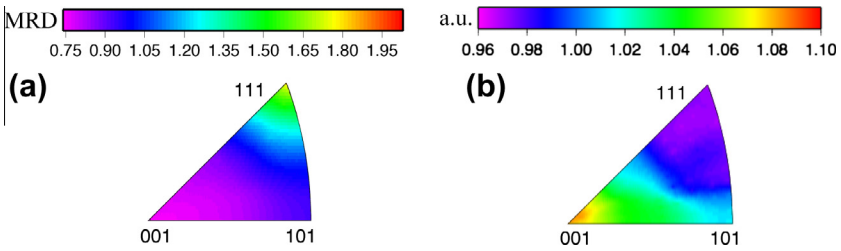

Fig. 3. The distribution of grain boundary planes (a) and energy (b) of the TWIP steel. MRD and a.u. are multiples of random distribution and arbitrary units, respectively.

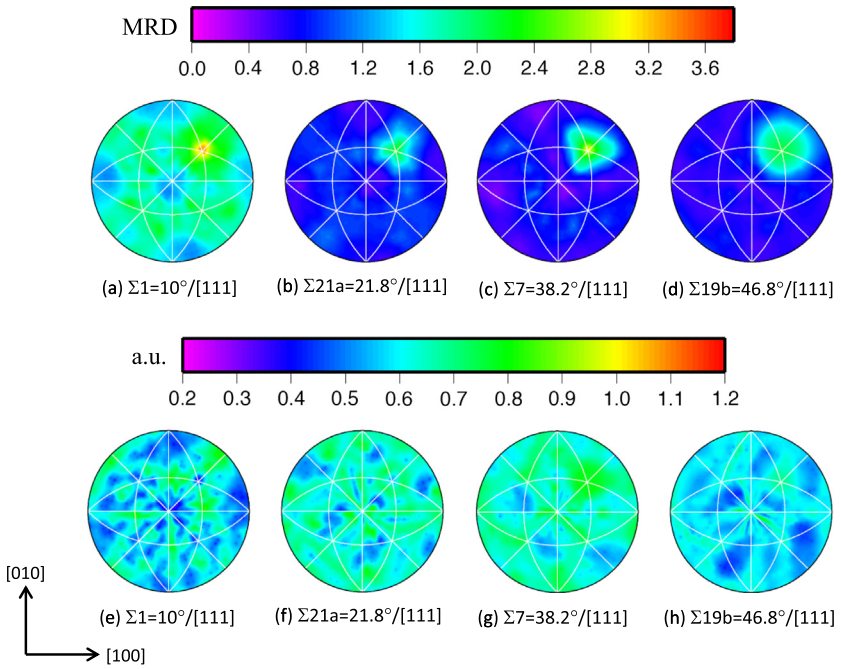

Fig. 4. (a–d) The distribution of grain boundary planes and (e–h) the corresponding grain boundary energy distribution at fixed misorientations of 10°/[111], 21.8°/[111], 38.2°/[111] and 46.8°/[111], respectively, plotted in stereographic projection along [001].

different at a misorientation of 38.9° about the [110] axis (Σ9). The most common boundaries are on the zone of pure tilt boundary positions with a maximum of ~2.7 MRD mainly centred on the (1 −1 4)‖(1 −1 4) symmetric tilt boundary (Fig. 6b). A moderate intensity is also apparent at the (−2 2 1)‖(−2 2 1) symmetric tilt boundary orientation. The distribution of grain boundary planes was slightly different when the misorientation angle increased to 50.5°. The position of the main maximum on the tilt boundary zone axis appeared at the (1 −1 3)‖(1 −1 3) symmetric tilt orientation, having a lower peak intensity of ~1.94 MRD (i.e. Σ11, Fig. 6c). Interestingly, the energy distributions revealed a strong inverse correlation with the corresponding populations for all misorientation angles (Fig. 6). For example, the minima observed at the zone of pure tilt boundaries generally

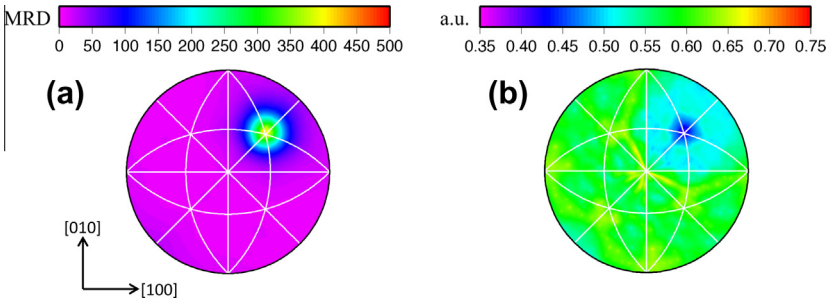

Fig. 5. (a) The distribution of grain boundary planes and (b) the corresponding grain boundary energy distribution at a fixed misorientation of 60°/[1 1 1], plotted in stereographic projection along [0 0 1].

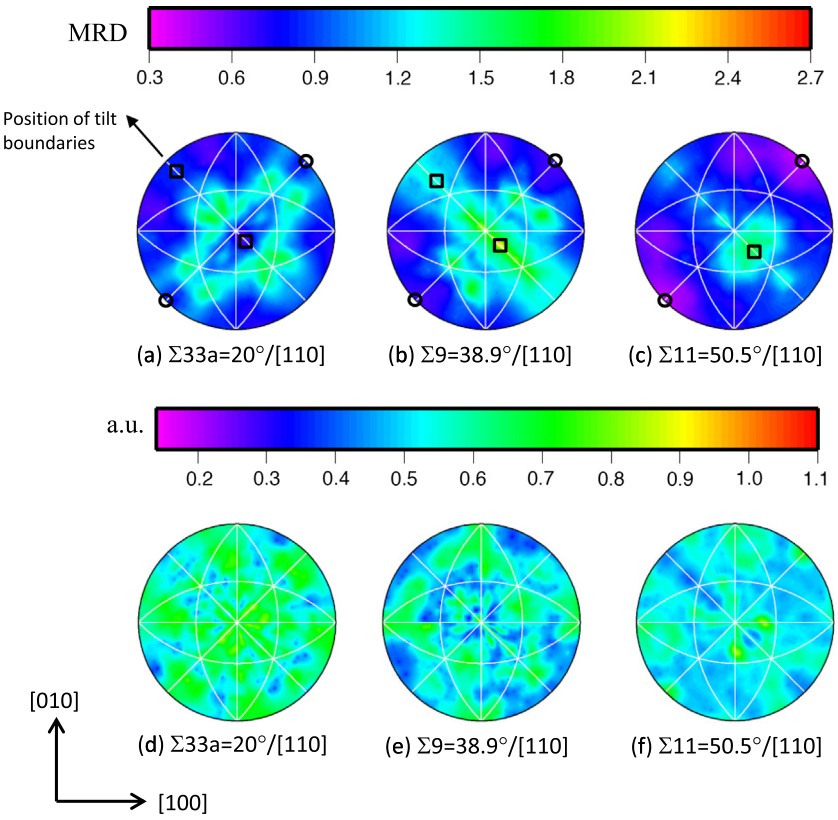

Fig. 6. (a–c) The distribution of grain boundary planes and (d–f) the corresponding grain boundary energy distribution at the fixed misorientations of 20°/[1 1 0], 38.9°/[1 1 0] and 50.5°/[1 1 0], respectively, plotted in stereographic projection along [0 0 1]. The circle and square marks in (a–c) represent the position of twist and symmetric tilt boundaries, respectively.

occurred at maxima in the corresponding population distributions for both Σ9 and Σ11 boundaries (Fig. 6b, c, e, and f). There were, however, a few deep minima in the energy distributions for Σ9 and Σ11 boundaries, which did not appear as highly populated regions in the corresponding distributions.

Grain boundaries with misorientations around [1 0 0] were much less frequently observed than those with misorientations about the [1 1 0] or [1 1 1] axes (Fig. 7). There were only a few grain boundary plane orientations with populations >1 MRD (i.e. Σ25a, Fig. 7a). Other boundaries had populations ⩽0.8 MRD (e.g. Σ5, Fig. 7b). The distribution of grain boundary planes for the Σ25a misorientation appeared as multiple peaks on the {1 1 1} positions with maxima of 1.8 MRD (Fig. 7a). The distribution of grain boundary planes slightly changed for higher misorientation angles showing more peaks about the {1 1 1} and {1 1 0} positions, although the populations were much lower (Fig. 7b). In general, boundaries with [1 0 0] misorientations were rare. For example, the average population was 1.27 MRD and 0.48 MRD for the Σ25a and Σ5 boundaries, respectively. Similar to other misorientations, the grain boundary energy distributions were inversely correlated with the corresponding populations (Fig. 7). However, the boundaries with [1 0 0] misorientations mostly revealed much higher energies compared with other misorientations.

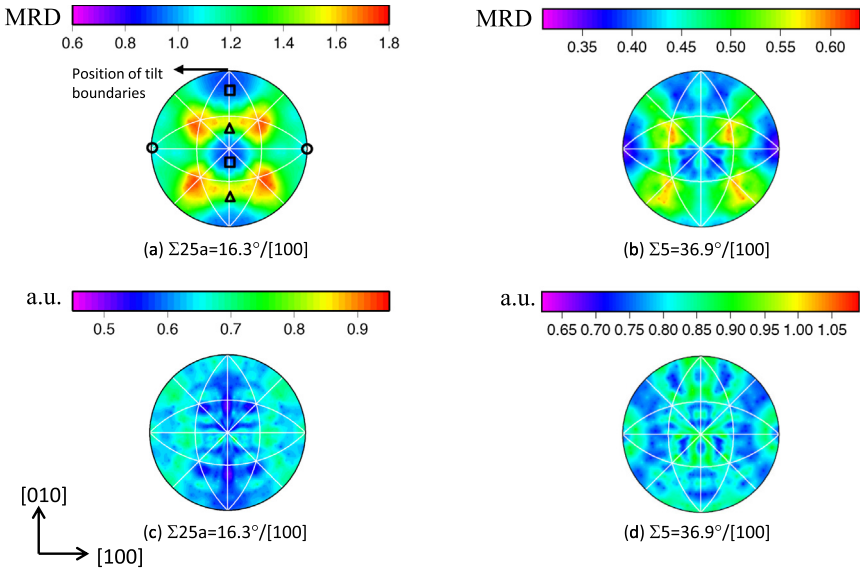

Fig. 7. (a–e) The distribution of grain boundary planes and (f–j) the corresponding grain boundary energy distribution at the fixed misorientations of 16.3°/[100] and 36.9°/[100], respectively, plotted in stereographic projection along [001]. The circle, square and triangle marks in (a) represent {100} twist, {031} tilt and {012} tilt boundaries, respectively.

The average energies of the Σ25a and Σ5 boundaries were 0.65 a.u. and 0.85 a.u., respectively. In comparison, the average energy was ~0.6 a.u. for most boundaries with [111] misorientations (e.g. Σ3, Fig. 5b).

The twist boundary populations and energies for all misorientation axes along the edges of the standard stereographic triangle are shown in Fig. 8. The horizontal lines for each misorientation axis represent the population and energy of twist boundaries as a function of twist angle in Fig. 8a and b, respectively. The peaks observed in Fig. 8 can be closely connected to the grain boundary character and energy distributions presented in Figs. 4–7. There were peaks with moderate intensity on the left-hand side of the population plot, representing low-misorientation-angle boundaries (i.e. labelled as "LA" in Fig. 8, $\theta < 15°$). In comparison, these regions appeared as low-energy locations in Fig. 8b. Two strong peaks for 60° and 180° about the ⟨111⟩ axis were the coherent twin boundaries (i.e. Σ3) shown in Fig. 5a. Multiple moderate peaks also appeared about the ⟨111⟩ axis (Fig. 8a), which are twist boundaries as observed in Fig. 4a–d. There were also two twist boundary peaks about [−311] and [201] at 150° and 130°, respectively. The twist boundaries energy plot was, however, more complex compared with the twist boundary population (Fig. 8). In general, there was an inverse relationship between twist boundary energy and population, where the twist boundaries with high population appeared to have low to moderate energy, behavior similar to, for example, coherent twin boundaries (Fig. 8).

Fig. 9 summarizes the results from the observations of grain boundary population and energy, where the average relationship between the two quantities is plotted. In the present analysis, the grain boundary energies were categorized into equally spaced bins with a width of 0.05 a.u., and

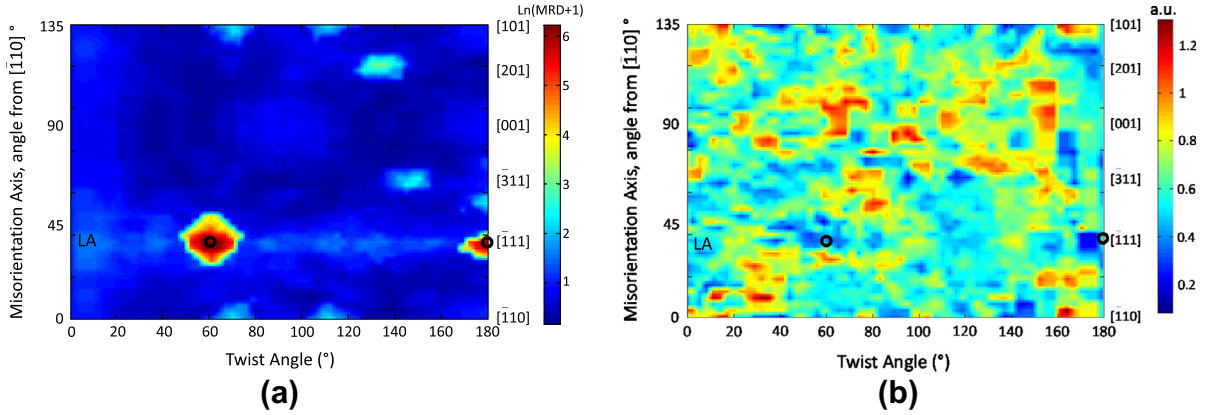

Fig. 8. Twist boundary populations (a) and energies (b) for all misorientation axes on the edges of the standard stereographic triangle. LA shows the positions of low misorientations. MRD and a.u. are multiples of random distribution and arbitrary units, respectively. Open circles in (a) and (b) represent the coherent twist boundary positions.

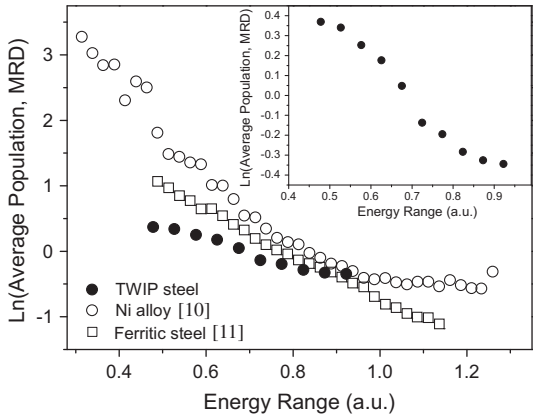

Fig. 9. The average relationship between the grain boundary population and energy for different materials. Inset is the grain boundary population vs. energy for the TWIP steel. The grain boundary energies for the TWIP steel were classified into equally spaced bins with a width of 0.05 a.u.

the average population of all boundaries in a given bin was calculated. The current observations illustrate that, on average, a very strong inverse correlation exists between the grain boundary population and the relative grain boundary energy in the high-manganese austenitic TWIP steel.

4. Discussion

The ability to measure all five independent crystallographic grain boundary parameters in the current study enables us to comprehensively survey the relative grain boundary area and energy distributions in the austenitic TWIP steel. One of the most interesting results is the presence of a very strong inverse relationship, on average, between the relative grain boundary population and corresponding grain boundary energy. In other words, the boundaries with the highest population have the lowest energy, while the less frequently observed boundaries, in contrast, show high energy (Figs. 3–9). This is consistent with recent observations for materials with different crystal structures (e.g. yttria [9], Ni [10] and ferrite [11]) and various simulations [32–35].

However, when the relationships between ln(population) and energy are compared, there are significant differences between the different materials (Fig. 9). For example, the relationship for the ferritic steel is nearly linear, whereas there is curvature in the results for the Ni and TWIP steel. There are several reasons for these differences. First, the widths of the relative area distributions differ in each case, with Ni spanning the largest range and the ferritic steel spanning the smallest. Second, the energy scale is relative for each material and cannot reflect the absolute differences in grain boundary energy that must exist between the materials. Finally, multiple twinning, which influences the misorientation distribution, can influence the relationship by selectively altering the population in certain energy classes. We note that while the misorientation distributions of the TWIP steel and the Ni were both affected by twinning, the most nearly linear relationship in Fig. 9 is for the ferritic steel that had a random misorientation distribution. This is consistent with simulations assuming a random misorientation distribution [32–35].

In general, the relative grain boundary area and energy for the TWIP steel are similar to those reported results for other fcc materials (e.g. Ni [10]), suggesting that the grain boundary characteristics (i.e. GBCD and GBED) strongly depend on the crystal structure [36]. Similar to other fcc materials, the Σ3 annealing twin grain boundary with symmetric twist characteristics has the highest population in the austenitic TWIP steel and also appears to have the lowest energy among other CSL boundaries (Fig. 5). The analysis of present planar section data reveals that the current TWIP boundary population consisted of 75.3% and 24.7% non-Σ3 and Σ3 boundaries, respectively. In terms of length, the Σ3 boundaries make up ~28.5% of total boundary length. However, not all Σ3 boundaries within Brandon's criterion [37] represent coherent Σ3 boundaries. Here, the boundary segments within ±10° deviation from the orientation of the ideal twin plane are considered as coherent Σ3 boundaries. Based on this criterion, the coherent Σ3 boundaries make up 9.7% and 14.6% of the population and the length of total boundaries, respectively. Recently, the coherent twin boundary was measured to be 28.6% of the total grain boundary length in a high-purity Ni alloy using a similar approach [10]. This is about twice as high as the measured value in the current study.

As mentioned earlier, multiple twinning is common during the microstructure evolution (i.e. recrystallization and/or grain growth) of fcc materials. One example of multiple twinning is the formation of the Σ9 boundary, resulting from the meeting of two Σ3 boundaries which do not share a common rotation axis. In the current study, the Σ9 grain boundary population is relatively low compared with other fcc materials, making up only 1.5% of all of the grain boundary length. However, its relative area distribution was consistent with other reports, revealing maxima along the zone of tilt boundaries [10,38,39]. There is also a strong correlation between population maxima and corresponding energy minima positioning at the {1 1 4} symmetric tilt boundary (Fig. 6b and e).

This difference in the population of CSL boundaries (i.e. Σ3 and Σ9) between Ni and the current TWIP steel can be due to different factors, such as texture, grain morphology (i.e. formation mechanism [40,41]), grain size [42] and composition (i.e. SFE [43]). Interestingly, both materials were produced through static recrystallization, resulting in relatively similar texture and grain morphology (i.e. equiaxed). On the other hand, the twin population is expected to increase with a decrease in the grain size [42]. However, this is not consistent with the current result as the Ni grain size was ~11 μm [10], which is much coarser than the TWIP steel (i.e. 2.5 μm), though showing a greater twin population. To explain the strong difference in the CSL

population of the TWIP steel it would therefore be necessary to examine the effect of the composition on the population of CSL grain boundaries.

There is a significant difference in the SFE of the Ni alloy (i.e. 128 mJ m^{-2} [28]) and the TWIP steel (i.e. 25 mJ m^{-2} [29]) at room temperature. The materials with lower SFE are, in general, expected to have a greater CSL boundary population [43]. However, the current result reveals the opposite behaviour. This observation could arise from the distinct thermomechanical routes used for the production of the TWIP steel and Ni alloy. The former was subjected to ~60% cold rolling followed by 1 min annealing at 800 °C, resulting in a fully statically recrystallized equiaxed grain structure. The SFE of the TWIP steel becomes larger with an increase in temperature [44,45]. For the current steel composition, the SFE is calculated for different temperatures using a thermodynamic approach proposed in Ref. [45]. The SFE is increased significantly from ~29 mJ m^{-2} at room temperature to ~230 mJ m^{-2} at 800 °C, which would greatly exceed that of Ni. On the contrary, it has been reported that the SFE of a Ni alloy decreases with an increase in temperature [46]. The Ni alloy was subjected to 70% cold reduction followed by annealing at 300–350 °C [10]. Under these conditions, the stacking fault energy of Ni should be reduced from 128 mJ m^{-2} at room temperature to ~124 mJ m^{-2} at the annealing temperature [46]. Comparing the SFE of the TWIP steel and Ni alloy at the temperature where their grain boundary structures were evolved through static recrystallization, it appears that the SFE of the TWIP steel is much greater than that of the Ni alloy. As a result, there is a lower CSL boundary population observed in the TWIP steel compared with the Ni alloy. This suggests that the thermomechanical processing routes/parameters (e.g. temperature) significantly influence the grain boundary character distribution.

Similar to the population, it appears that there is a difference between the relative grain boundary energy distribution in the TWIP steel and the Ni alloy measured by a similar approach. For example, the range of energies in the distribution of Σ3 in the TWIP steel (i.e. 0.35–0.75 a.u., Fig. 5b) is smaller than that of the Ni alloy (i.e. 0.33–0.933 a.u. [10]). As the measured energy is relative in the current study, it is not possible to draw a conclusion about absolute energy values. However, assuming that the average energies of boundaries in the two materials are the same, it can be concluded that the twins in the Ni alloy have the lower energy in comparison with the current TWIP steel. This could arise from the high alloying addition present in the current TWIP steel (i.e. C, Al and Mn).

Based on the current result, the measured grain boundary energies of [1 1 0] symmetric tilt boundaries are compared with the corresponding measured populations as a function of tilt angle in Fig. 10. Both the energy and population of symmetric tilt boundaries formed by rotation around the [1 1 0] misorientation axis reveal pronounced changes with the misorientation angle. The main energy

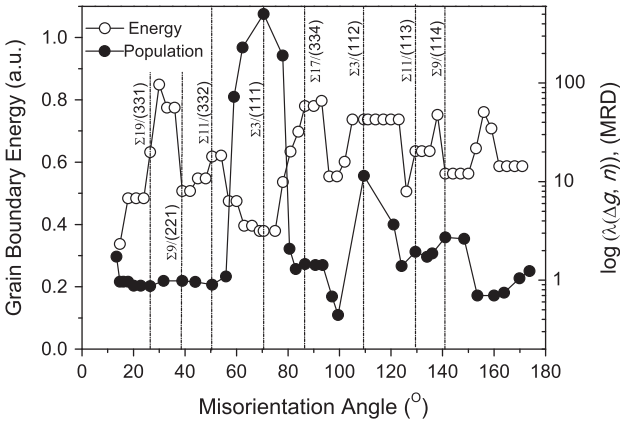

Fig. 10. Comparison of measured grain boundary energy to populations as a function of symmetric [1 1 0] tilt boundary misorientation angle.

cusps appear at the orientations of Σ3 = 109.5°/(1 1 2), Σ3 = 70.5°/(1 1 1) and Σ9 = 141°/(1 1 4), which are consistent with the previous work reported for different fcc materials through both measurements (Al [15,16], Cu [22]) and simulations (Cu and Al [48]). Interestingly, these positions are inversely correlated with the corresponding grain boundary populations, though the highest population relates to the coherent twin boundaries, Σ3, as shown in Fig. 5. The $(1\,-1\,4)\|(1\,-1\,4)$ symmetric tilt boundaries (i.e. Σ9) clearly appeared in the grain boundary plane distributions (Fig. 6b,e). The minima observed in the populations at 100° and 120° are inconsistent with the previous energy measurements for fcc materials and also do not reflect a high-energy boundary. These discrepancies could have arisen from the limited resolution of the current measurement (~10° bin size) or limitations related to the discretization, as discussed in Ref. [11]. In general, a comparison between the grain boundary energy and population with respect to the symmetric [1 1 0] tilt grain boundary misorientation angle shows a relatively strong point-to-point inverse relationship (i.e. the grain boundaries with high populations having low energies) as earlier reported for other materials through experimental studies (e.g. Al [47] and MgO [8]).

5. Conclusion

The five-parameter grain boundary character and energy distributions of a fully austenitic high-manganese steel were characterized using focused ion beam serial sectioning combined with EBSD. The grain boundary population and energy revealed a strong dependence on both the grain boundary plane orientation and lattice misorientation. The grain boundary planes with the (1 1 1) orientation had the largest relative areas and minimum energy, when misorientation is ignored. The most commonly observed boundaries were {1 1 1} symmetric twist boundaries with a Σ3 misorientation. These boundaries also had relatively low energies. There was, on average, a

strong inverse correlation between the relative areas of different types of grain boundaries and the relative grain boundary energies. The current results from the TWIP steel were compared to those of high-purity Ni. In general, it was found that the polycrystals with the same atomic structure have very similar GBCD and GBED characteristics.

Acknowledgements

Prof. B.C. De Cooman is thankfully acknowledged for providing the TWIP steel. The work at Deakin University was supported through the grants provided by the Australian Research Council. H.B. is also grateful for the financial assistance granted by Outside Study Program of Deakin University. Financial support at Carnegie Mellon from the ONR-MURI under the grant no. N00014-11-1-0678 is gratefully acknowledged; support for facilities by the MRSEC program of the National Science Foundation under Award Number DMR-0520425 is also acknowledged.

References

[1] Beladi H, Timokhina IB, Estrin Y, Kim J, De Cooman BC, Kim SK. Acta Mater 2011;59:7787–99.
[2] Remy L, Pineau A. Mater Sci Eng 1976;26:123.
[3] Mahajan S, Chin GY. Acta Metall 1973;21:1353.
[4] Christian JW, Mahajan S. Prog Mater Sci 1995;39:1.
[5] Karaman I, Sehitoglu H, Gall K, Chumlyakov YI, Maier HJ. Acta Mater 2000;48:1345.
[6] Beladi H, Cizek P, Hodgson PD. Acta Mater 2010;58. 3531-35-41.
[7] Kashyap BP, Tangri K. Acta Mater 1997;45:2383.
[8] Saylor DM, Morawiec A, Rohrer GS. Acta Mater 2003;51:3675.
[9] Dillon SJ, Rohrer GS. J Am Ceram Soc 2009;92:1580.
[10] Li J, Dillon SJ, Rohrer GS. Acta Mater 2009;57:4304.
[11] Beladi H, Rohrer GS. Acta Mater 2013;61:1404–12.
[12] Rohrer GS, Saylor DM, El Dasher B, Adams BL, Rollett AD, Wynblatt P. Z Metallkd 2004;95:197.
[13] Read WT, Shockley W. Phys Rev 1950;78:275.
[14] Gjostein NA, Rhines FN. Acta Metall 1959;7:319.
[15] Hasson GC, Goux C. Scripta Metall 1971;5:889.
[16] Hasson G, Boos J-Y, Herbeuval I, Biscondi M, Goux C. Surf Sci 1972;31:115.
[17] McLean M. J Mater Sci 1973;8:571.
[18] Chan S-W, Balluffi RW. Acta Metall 1985;33:1113.
[19] Chan S-W, Balluffi RW. Acta Metall 1985;34:2191.
[20] Schmelzle R, Muschlik T, Gust W, Predel B. Scripta Metall Mater 1991;25:1981.
[21] Wolf U, Ernst F, Muschik T, Finnis MW, Fischmeister HF. Philos Mag A 1992;66:991.
[22] Miura H, Kato M, Mori T. J Mater Sci Lett 1994;13:46.
[23] Straumal BB, Polyakov SA, Bischoff E, Gust W, Mittemeijer EJ. Interface Sci 2001;9:287.
[24] Skidmore T, Buchheit RG, Juhas MC. Scripta Mater 2004;50:873.
[25] Amouyal Y, Rabkin E, Mishin Y. Acta Mater 2005;53:3795.
[26] Barmak K, Kim J, Kim C-S, Archibald WE, Rohrer GS, Rollett AD, et al. Scripta Mater 2006;54:1059.
[27] Amouyal Y, Rabkin E. Acta Mater 2007;55:6681.
[28] Humphreys FJ, Hatherly M. Recrystallization and related annealing phenomena. 2nd ed. Oxford: Elsevier; 2004.
[29] Sato K, Ichinose M, Hirotsu Y, Inoue Y. ISIJ Int 1989;29:868.
[30] Morawiec A. Acta Mater 2000;48:3525.
[31] Vercammen S, Blanpain B, De Cooman BC, Wollants P. Acta Mater 2004;52:2005.
[32] Gruber J, George DC, Kuprat AP, Rohrer GS, Rollett AD. Scripta Mater 2005;53:351.
[33] Rohrer GS, Gruber J, Rollett AD. In: Rollett AD, editor. Applications of texture analysis. Ceram Trans, vol. 201. Hoboken, NJ: John Wiley; 2009. p. 343–54.
[34] Gruber J, Rohrer GS, Rollett AD. Acta Mater 2010;58:14.
[35] Dillon SJ, Rohrer GS. Acta Mater 2009;57:1.
[36] Holm EA, Rohrer GS, Foiles SM, Rollett AD, Miller HM, Olmsted DL. Acta Mater 2011;59:5250.
[37] Brandon DG. Acta Metall 1966;14:1479.
[38] Rohrer GS, Randle V, Kim CS, Hu Y. Acta Mater 2006;54:4489.
[39] Randle V, Jones R. Mater Sci Eng A 2009;524:134.
[40] Beladi H, Rohrer GS, Rollett AD, Tari V, Hodgson PD. Acta Mater 2014;63:86.
[41] Randle V, Rohrer GS, Hu Y. Scripta Mater 2008;58:183.
[42] Watanabe T, Fujii H, Oikawa H, Arai KI. Acta Metall 1989;37:941.
[43] Randle V. Acta Mater 1999;47:4187.
[44] Allain S, Chateau JP, Bouaziz O, Migot S, Guelton N. Mater Sci Eng A 2004;387–389:158.
[45] Saeed-Akbari A, Imlau J, Prahl U, Bleck W. Metall Mater Trans A 2009;40:3076.
[46] Shang SL, Zacherl CL, Fang HZ, Wang Y, Du Y, Liu ZK. J Phy Condens Matter 2012;24:1.
[47] Saylor DM, El Basher BS, Rollett AD, Rohrer GS. Acta Mater 2004;52:3649.
[48] Tschopp MA, Spearot DE, Mcdowell DL. In: Hirth JP, editor. Dislocations in solids. Amsterdam: Elsevier; 2008. p. 43–97.